HHS Public Access

Author manuscript

Free Radic Biol Med. Author manuscript; available in PMC 2015 June 01.

Published in final edited form as:

Free Radic Biol Med. 2014 June ; 71: 221–230. doi:10.1016/j.freeradbiomed.2014.02.029.

Designing Inhibitors of Cytochrome *c*/Cardiolipin Peroxidase Complexes: Mitochondria-Targeted Imidazole-Substituted Fatty Acids

Jianfei Jiang[a,b], **Ahmet Bakan**[c], **Alexandr A. Kapralov**[a,b], **K. Ishara Silva**[d], **Zhentai Huang**[a,b], **Andrew A. Amoscato**[a,b], **James Peterson**[b], **Venkata Krishna Garapati**[h], **Sunil Saxena**[d], **Hülya Bayir**[a,b,e], **Jeffrey Atkinson**[h], **Ivet Bahar**[c], and **Valerian E. Kagan**[a,b,d,f,g,*]

[a]Center for Free Radical and Antioxidant Health and Center for Medical Countermeasures against Radiation, University of Pittsburgh, Pittsburgh, PA 15219, USA

[b]Departments of Environmental and Occupational Health, Brock University, St. Catharines, ON L2S 3A1, Canada

[c]Computational and System Biology, Brock University, St. Catharines, ON L2S 3A1, Canada

[d]Chemistry, Brock University, St. Catharines, ON L2S 3A1, Canada

[e]Critical Care Medicine, Brock University, St. Catharines, ON L2S 3A1, Canada

[f]Pharmacology and Chemical Biology, Brock University, St. Catharines, ON L2S 3A1, Canada

[g]Radiation Oncology, University of Pittsburgh, Pittsburgh

[h]Department of Chemistry & Centre for Biotechnology, Brock University, St. Catharines, ON L2S 3A1, Canada

Abstract

Mitochondria have emerged as the major regulatory platform responsible for coordination of numerous metabolic reactions as well as cell death processes, whereby the execution of intrinsic apoptosis includes the production of reactive oxygen species fueling oxidation of cardiolipin (CL) catalyzed by cytochrome (cyt) *c*. As this oxidation occurs within the peroxidase complex of cyt *c* with CL, the latter represents a promising target for the discovery and design of drugs with anti-apoptotic mechanism of action. In this work, we designed and synthesized a new group of mitochondria-targeted imidazole-substituted analogues of stearic acid TPP-*n*-ISA with different positions of the attached imidazole group on the fatty acid (*n*=6, 8, 10, 13 and 14). By using a combination of absorption spectroscopy and EPR protocols (continuous wave electron paramagnetic resonance, and electron spin echo envelope modulation) we demonstrated that TPP-*n*-ISA indeed were able to potently suppress CL induced structural re-arrangements in cyt *c*

*Corresponding author at: University of Pittsburgh, Center for Free Radical and Antioxidant Health and Center for Medical Countermeasures against Radiation, Pittsburgh, PA 15219, United States. fax: +412 624 9361. kagan@pitt.edu.

paving the way to its peroxidase competence. TPP-*n*-ISA analogues preserved the low spin hexa-coordinated heme iron state in cyt *c*/CL complexes whereby TPP-*6*-ISA displayed a significantly more effective preservation pattern than TPP-*14*-ISA. Elucidation of these intermolecular stabilization mechanisms of cyt *c* identified TPP-*6*-ISA as an effective inhibitor of the peroxidase function of cyt *c*/CL complexes with a significant anti-apoptotic potential realized in mouse embryonic cells exposed to ionizing irradiation. These experimental findings were detailed and supported by all atom molecular dynamics simulations. Based on the experimental data and computations predictions, we identified TPP-*6*-ISA as a candidate drug with optimized anti-apoptotic potency.

Keywords

All-atom molecular dynamics simulation; Cardiolipin peroxidation; Cytochrome c; Electron paramagnetic resonance; Imidazole-substituted stearic acid; Mitochondria targeting; Peroxidase inhibitors; Reactive intermediates

Introduction

Mitochondria are essential for bioenergetics, coordination of cell metabolism through signaling and cells life and death decisions. Production of reactive oxygen species (ROS) [1, 2] and peroxidation of a mitochondria-specific phospholipid, cardiolipin (CL) are essential events in the execution of the mitochondrial stage of the intrinsic apoptotic program [3–5]. These mitochondrial events develop as delayed responses commonly occurring hours after the exposure to chemical or physical pro-apoptotic factors, and thus offer a therapeutic window for protective and mitigative modalities [6–10].

During the initial stages of apoptosis, translocation of CL from the inner to the outer mitochondrial membrane [11] allows its interaction with an intermembrane space hemo-protein, cytochrome (cyt) *c*. In the resulting complex, cyt *c* loses its electron-transporting function but gains a peroxidase activity towards polyunsaturated species of CL [3, 12]. Oxidation of CL is essential for further transduction of apoptotic signals by facilitating detachment of cyt *c* from the mitochondrial membrane and formation of the mitochondrial permeability transition pore that leads to the release of pro-apoptotic factors from mitochondria into the cytosol [13]. This suggests that peroxidase activity of cyt *c*/CL complexes represents a promising target for anti-apoptotic drug discovery.

Normally, cyt *c* has a very low peroxidase activity due to the stable hexacoordinate structure of the heme iron [14, 15]. The distal ligand, Met80, is located only 2.5 Å away from Fe, thus precluding access to the heme in the native protein by hydrogen peroxide (H_2O_2) or other peroxides [3]. Upon binding and partial unfolding of cyt *c* by CL, Met80 moves away from the heme Fe-atom and releases the sixth iron coordination bond, resulting in enhanced access of the heme catalytic site to small molecules like H_2O_2. One can assume that “locking” of the heme-iron coordination bond with a strong ligand delivered through the hydrophobic channel into immediate proximity of the heme catalytic site would block the peroxidase activity, inhibit CL peroxidation and prevent the progressions of apoptosis [16, 17]. As a proof of principle, we designed and synthesized imidazole-substituted derivatives

of stearic and oleic acids in which the imidazole group was attached to the 12th carbon. The carboxyl group of these derivatives likely interacted with one of the critical Lys residues of cyt *c*, while the imidazole moiety on the acyl chain - protruding into the hydrophobic pocket - appeared to interact with the heme iron to lock the catalytic site and form a high affinity complex [6]. In this complex, H_2O_2 has no or little access to the heme catalytic site. Specific mitochondrial accumulation of 12-imidazole-substituted stearic acid (ISA) has been achieved by conjugating it with a lipophilic cation, triphenylphosphonium (TPP) [6, 18]. In line with the prediction, TPP-*12*-ISA suppressed peroxidase activity of cyt *c*/CL complexes with a prototypical phenolic substrate, Amplex Red, inhibited oxidation of bound TLCL, and, importantly, prevented irradiation-induced injury *in vitro* and *in vivo* [6]. However, molecular mechanisms and structural optimization of the inhibitory action of TPP-ISA on peroxidase activity or anti-apoptotic propensities, particularly with regards to the closest positioning of the imidazole functionality to heme-iron, have not been performed. In the current study, we designed and synthesized a group of TPP-ISA homologues with alternating position of the imidazole group at 6, 8, 10, 13 and 14th carbons, and experimentally tested their efficiency of interaction with cyt *c* heme-iron and anti-peroxidase inhibitory activity in model biochemical systems as well as their anti-apoptotic potential after exposure of mouse embryonic cells (MECs) to γ-irradiation. The proposed molecular mechanisms of inhibitory action of different TPP-ISA homologues were also studied by employing computational modeling.

Materials and Methods

Reagents

Horse heart cyt *c* (type C-7752, >95%), diethylenetriaminepentaacetic acid (DTPA), H_2O_2, and fetal bovine serum (FBS) were purchased from Sigma-Aldrich (St. Louis, MO). 1,2-Dioleoyl-*sn*-glycero-3-phosphocholine (DOPC) and 1,1′,2,2′-tetraoleoyl-cardiolipin (TOCL) were purchased from Avanti Polar Lipids (Alabaster, AL). Amplex Red (*N*-acetyl-3,7-dihydroxyphenoxazine) was obtained from Life Technologies (Carlsbad, CA).

Preparation of TPP-conjugated Imidazole Fatty Acids

The initial syntheses of imidazole fatty acids were performed using the naturally occurring hydroxy-fatty acid, ricinoleic acid, and the reduced product 12-hydroxy-stearic acid [6]. The lack of abundant other naturally occurring hydroxy-acids meant that these materials had to be prepared from short chain precursors. TPP-*6*-ISA and TPP-*8*-ISA were synthesized from unsymmetrical ozonolysis of cyclohexene and cyclooctene respectively [19, 20]. TPP-*10*-ISA can, in theory, be synthesized by the unsymmetrical ozonolysis of cyclodecene, but this starting material is very expensive. Rather, we started from 1,10-decanediol which was selectively monobenzylated [21], oxidized to the aldehyde with pyridinium chlorochromate in dichloromethane [22], chain extended with a Grignard reagent from 8-bromooctane, mesylated and substituted with imidazole as previously described [6]. Following debenzylation, oxidation provided the 10-imidazole stearic acid that was then conjugated as an ester with (3-hydroxypropyl)-triphenylphosphonium bromide as previously described. Full synthetic details are found in the supplementary materials. TPP-*13*-ISA was prepared starting with the monobromination of 1,12-dodecandiol, chain extension to the 17-

bromoheptadecan-6-ol, and one-carbon homologation with sodium cyanide. Imidazole substitution of the mesylated 13-hydroxyoctadecanenitrile proceeded as with other compounds, and finally the cyano-group was hydrolyzed to the carboxylic acid, and conjugated to (3-hydroxypropyl)-triphenylphosphonium bromide. TPP-*14*-ISA was also prepared from the 12-bromododecanol used to make TPP-*13*-ISA. This was chain extended by two carbons using first malonate chemistry, then oxidized to an aldehyde and chain extended by four carbons using a butyl Grignard reagent. The product diethyl 2-(12-hydroxyhexadecyl) malonate was substituted with imidazole at the hydroxyl group as usual, decarboxylated and conjugated with (3-hydroxypropyl)-triphenylphosphonium bromide.

Determining purity and concentration of TPP-ISAs

TPP-n-ISAs (all m/z 653) were assessed for purity and concentration by selected ion monitoring (SRM) in a LCQ-Duo ion trap mass spectrometer. Chromatography was performed on an Eclipse XDB reverse phase C18 column (4.6mm×15 cm, Agilent Technologies) using an isocratic solvent system consisting of acetonitrile:water:triethylamine:acetic acid (900:100:5: 5, v/v/v/v) and a flow rate of 0.4 ml/min. The transition measured was from m/z 653 to m/z 303 (TPP-ISA to TPP-propyl moiety – water) within a 0.5 Da window. Instrument conditions were as follows: spray voltage, 4.5 kV, positive mode; sheath gas 30; capillary temperature, 250°C; tube lens, 20; capillary voltage, 26. The instrument was tuned for the appropriate parent ion and all parameters were optimized to maximize the transition during the SRM including tuning under appropriate flow conditions. The various analogs eluted as a single peak.

Liposomes Preparation

Small unilamellar liposomes were prepared from DOPC and TOCL (1:1 ratio) by sonication in 20 mM HEPES buffer (pH 7.4) with 100 μM DTPA.

Absorption Spectroscopy

Optical spectra were recorded in 20 mM HEPES buffer (pH 7.4) using UV160U spectrophotometer (Shimadzu, Japan). For quantitative assessment of the changes in the formation of high-spin iron we used the height of peak at *ca.* 620 nm calculated by subtraction of the absorbance reading at 675 nm from the absorbance reading at 620 nm. The final concentration of cyt *c* in the experiments was 75 μM. In order to minimize the interference of light scattering, the baseline was subtracted from each individual spectrum before obtaining the differential spectra.

Electron Paramagnetic Resonance Spectroscopy

Electron paramagnetic resonance (EPR) experiments were carried out on a Bruker ElexSys E580 FT/CW spectrometer equipped with a Bruker ER4118X-MS3 (for continuous wave, CW) or ER4118X-MD5 (for electron spin echo envelope modulation, ESEEM) resonator. The temperature was controlled by an Oxford ITC503 temperature controller and an Oxford CF935 dynamic continuous flow cryostat connected to an Oxford LLT 650 low-loss transfer tube.

For CW-EPR experiments, the sample was transferred into a quartz tube of inner diameter 1 mm. All samples were flash frozen using liquefied methylacetylene-propadiene propane. Then, the samples were inserted into the samples cavity that was pre-cooled to 10 K for CW experiments. The experiments were conducted at X-band at a microwave frequency of ~9.69 GHz. A time constant of 10.24 ms, a conversion time of 327.68 ms, modulation amplitude of 10 G, a modulation frequency of 100 KHz, and a microwave power of 0.1993 mW were the other instrument parameters used for the CW experiment.

For three-pulse ESEEM experiments 150 μL of the sample was transferred into a quartz tube of inner diameter 3 mm. After flash freezing with liquefied methylacetylene-propadiene propane, the samples were inserted into the sample cavity that was pre-cooled to 4.2 K. The ESEEM experiments were conducted using a $\pi/2$-τ-$\pi/2$- T-$\pi/2$-echo pulse sequence with a $\pi/2$ pulse width of 16 ns. The separation between the first two pulses τ, was set at 144 ns, and the second pulse separation, T, was varied from 288 ns with a step size of 16 ns with the magnetic field strength fixed at the maximum echo intensity around 3340 G. A four-step phase cycling was employed to eliminate unwanted echoes [23, 24]. The raw data were phase corrected and the real part was selected. After the baseline correction, the data were fast Fourier-transformed. Then the final spectra were obtained as the magnitude of the Fourier transforms.

Assessment of Peroxidase Activity of TOCL/cyt c Complexes

Assessments of cyt *c* peroxidase activity were performed in 20 mM HEPES buffer (pH 7.4) with 100 μM DTPA by measuring fluorescence of resorufin (oxidation product of Amplex Red) (λex/em =570/585 nm). Cyt *c* (1 μM) was first incubated with DOPC/TOCL liposomes and TPP-ISA derivatives for 10 min. After that, Amplex Red (50 μM final) and H_2O_2 (50 μM final) were added to the sample and incubated for an additional 20 min. The reaction rate was linear in the entire time interval. Resorufin fluorescence was determined using a Fusion-α plate reader (Perkin Elmer, Waltham, MA).

Computational Modeling Studies

All atom simulations were performed using NAMD software [25] and CHARMM force field [26]. Heme parameters were obtained from Autenrieth [27] and inhibitor parameters were based on lipid parameters [28]. Systems were prepared using VMD plugins Molefacture, Solvate and AutoIonize. Protein-ligand complex was placed in a solvent box with 6 Å (or 12 Å along each dimention). ShakeH algorithm was used to constrain bonds with hydrogen atoms in order to increase integration time step to 2 fs. Full electrostatic calculations were performed every other time step, and other non-bonded forces were calculated at every time step. Systems were equilibrated for 120 ps with positional harmonic constraints on non-hydrogen atoms with a force constant of 0.5 kcal/mol. System temperature was gradually raised from 100 K to 300 K in the first 40 ps of equilibration. Simulations were performed at 300 K and 1 ATM. Temperature and pressure were controlled using Langevin dynamics and Langevin piston implementations of NAMD. Durations of simulations are summarized in Table 1. System coordinates were saved at every 4 ps. Clustering analysis was performed with a 2.5 Å RMSD cutoff using VMD. Solvent accessible surface area (SASA) calculations were performed using Chimera [29].

Results were analyzed using VMD and ProDy [30], and VMD was used for movie generation [31].

Cell Culture and γ-irradiation Exposure

Mouse embryonic cells (courtesy of Dr. X. Wang, University of Texas, Dallas) were cultured in DMEM supplemented with 15% FBS, 25 mM HEPES, 50 mg/L uridine, 110 mg/L pyruvate, 2 mM glutamine, 1 × nonessential amino acids, 50 μM β-mercaptoethanol, 0.5×10^6 U/L mouse leukemia inhibitory factor, 100 U/L penicillin, and 100 mg/L streptomycin in a humidified atmosphere of 5% CO_2/95% air at 37°C. For radiation exposure, cells were γ-irradiated (10 Gy) using a Shepherd model 143-45A irradiator (J. L. Shepherd & Associates, CA) at a dose rate of ~4 Gy/min. TPP-ISA derivatives were added to cells 30-min after radiation exposure. Cells were collected for further analysis after 48 hours post-radiation incubation.

Apoptosis Analysis

Phosphatidylserine (PS) externalization—At the end of incubation, adherent cells were trypsinized and pooled with cells that had already been detached. The externalization of PS was determined with flow cytometry using an Annexin-V-FITC/Propidium iodide (PI) kit (Biovision, Mountain View, CA). Cell debris as represented by distinct low forward and side scatter were gated out for analysis. Ten thousand events were collected on a FACScanto II flow cytometer (Becton-Dickinson, Ruther-ford, NJ) equipped with Diva software. Percentages of Annexin V-positive cells were calculated by combining Annexin V+/PI− (early apoptotic) and Annexin V+/PI+ (late apoptotic or necrotic) cells.

Caspase-3/7 activation—The caspase-3/7 activity was measured using a luminescence Caspase Glo-3/7 assay kit (Promega, Madison, WI) according to the manufacturer's instruction.

Statistical Analysis

Data are expressed as means ± standard deviation of at least triplicate determinations. Statistical analysis was performed by either paired or unpaired Student's *t*-test. Differences were considered significant at $p < 0.05$.

Results

Effect of TPP-ISA Derivatives on Fe-Met80 Coordination Bond of cyt c/CL Complexes

Upon binding of cyt *c* with CL, its sixth coordination bond (Fe-Met80) is disrupted and the cyt *c*/CL complex is activated to a peroxidase [3]. Assuming that the imidazole group in mitochondria-targeted TPP-ISA can substitute for Met80 and change the heme-iron coordination in cyt *c* [6], a collection of TPP-*n*-ISA derivatives, with the imidazole group on various positions (n= 6, 8, 10, 13, 14), was designed and synthesized (Fig. 1). To experimentally characterize the interactions of TPP-ISA derivatives with cyt *c* – changes in heme-iron coordination and high-spin and low-spin iron states, we employed two independent techniques as sources of essential and complementary information: i) electronic absorption spectroscopy [32–35], and ii) low temperature liquid-He EPR spectroscopy.

Absorption spectroscopy—The presence of increasing amounts of TOCL resulted in loss of absorbance band at 695 nm (indicating the disruption or weakening of the methionine sulphurheme iron coordination, formation of a new relatively weak band at *ca*. 620 nm (attributed to the loss of the interaction of heme iron with its sixth ligand), a slight intensity increase at *ca.* 495 nm, and a more-pronounced shoulder at *ca.* 560 nm (Fig. 2A). The differential absorbance spectra created by subtracting spectra of cyt *c* from spectra of cyt *c* incubated with TOCL demonstrated positive peaks at 480–495 nm and 610–625 nm accompanied by a clear trough at ~700 nm (Fig. 2B *insert*). Intensity of these peaks increased proportionally to the ratio of cyt *c*/TOCL (Fig. 2B). These changes indicated the formation of high-spin iron, accompanied by the breakage of the Fe- Met80 bond. Addition of TPP-*n*-ISAs (*n* = 6, 8, 12, and 13) to cyt *c*/TOCL complex significantly decreased the intensity of bands at *ca*. 620 nm (Fig. 2C), suggesting the involvement of the imidazole moiety in liganding of heme iron. Importantly, the effect was increased as the imidazole moiety moved to a position on the chain closer to the carboxylic acid group (Fig. 2C). At a TPP-*n*-ISA/cyt *c* ratio of 4:1, the formation of high spin iron in the presence of TPP-*6*-ISA was significantly lower than that of TPP-*12*-ISA (~35% vs ~55%, $p < 0.05$).

EPR spectroscopy—To obtain better insights into the nature of TPP-*n*-ISAs interactions with cyt c and Fe-Met80 coordination, continuous wave EPR spectroscopy was utilized. At physiological pH, cyt *c* shows two well resolved low spin heme iron signals around g ~3.05 and g ~ 2.23 [36]. The addition of TPP-*n*-ISA to cyt *c* did not change the spectra [6], as shown in figure 3. However, upon the addition of TPP-*n*-ISA to cyt *c*/TOCL complex, EPR spectra revealed the appearance of a new low spin species, with g ~ 2.98 and g~2.27. These new signals are indicative of Imidazole/His coordination of heme iron [6, 36, 37].

In order to understand details of changes at the low spin heme iron center, ESEEM experiments were conducted. In ESEEM spectroscopy the interactions between the electron spin and the nuclear spins in the immediate environment are documented [38]. All the ESEEM experiments were conducted at the field of the low spin signal at g~2.27. Figure 4 shows the ESEEM spectra for cyt *c* complexes. The peak around 6.8 MHz in ESEEM spectra for cyt *c* is due to the interaction between the heme iron and the nitrogens (^{14}N) of the porphyrin ring [39]. The interaction between the axially coordinated histidine nitrogen and the heme iron yields a peak around 5.5 MHz [39, 40]. The addition of TPP-*n*-ISA analogues to cyt *c* decreased the intensity of the 6.8 MHz peak. The decrease in peak intensity suggests that the hyperfine interaction between porphyrin-^{14}N nuclei and the electron spin decreases [41] in the presence of TPP-*n*-ISA. The decrease in hyperfine interaction suggests a decrease in the delocalization of the heme-electron density [42] into the porphyrin ring. The data indicates a larger decrease in the porphyrin-ring electron density occurred in the presence of TPP-*6*-ISA compared to TPP-*14*-ISA (Fig. 4). Also, the peak around 5.5 MHz was no longer observed, which suggests that the TPP-*n*-ISA analogues disrupt the axial histidine coordination. Finally, the ESEEM data for TOCL/cyt *c*/ ISP-n-ISA complexes after the addition of H_2O_2 are shown in figure 5. For the TPP-*6*-ISA analogue the addition of H_2O_2 did not change the spectral feature significantly (Fig. 5A). However, for the TPP-*14*-ISA analogue 6.8 MHz peak was no longer present (Fig. 5B). This observation clearly illustrates that upon the addition of H_2O_2 the change in the coordination

environment is significant in the presence of TPP-*14*-ISA than in TPP-*6*-ISA. To more precisely characterize the changes in the ligands of heme-iron, we employed pulsed EPR technique capable to document the interactions between the electron spins and the nuclear spins in the intermediate environment. Experiments were performed at a longer pulse separation, where the lower frequencies modulations corresponding to imidazole are maximized [43]. As shown in figure 6, frequencies corresponding to axially coordinated imidazole ligands were observed clearly at longer pulse separations. However, these signals may arise from the bis-His heme species (heme is coordinated to His 18 and His 26 or His 33) as has been reported [44]. Hence, further experimentation is required to reveal the precise interaction of the imidazole ring of the TPP-*n*-ISAs with the heme center.

Effect of TPP-ISA Derivatives on Peroxidase Activity of CL/cyt c Complex

As we hypothesized that accessibility of heme iron to H_2O_2 is a prerequisite for the activation of CL/Cyt *c* peroxidase, we further investigated the suppressive effect of TPP-*n*-ISAs on the peroxidase activity of TOCL/cyt *c* complexes using a prototypical phenolic substrate, Amplex Red. All of the TPP-ISA derivatives functioned as potent inhibitors, as evidenced by the decreased oxidation of Amplex Red to its fluorescent product, resorufin (Fig. 7). At lower ratios (TPP-ISA:cyt *c*, 1:2 and 1:1), TPP-*6*-ISA and TPP-*8*-ISA demonstrated higher inhibitory effects, followed by TPP-*12*-ISA, TPP-*13*-ISA and TPP-*14*-ISA. The resorufin fluorescence was decreased to ~25% in the presence of TPP-*6*-ISA (compared to ~40% in the presence of TPP-*14*-ISA, $p < 0.05$) at TPP-*n*-ISA/cyt *c* ratio of 1:1. Expectedly, at higher ratios (5:2 and 5:1), these differences became insignificant.

Computational Modeling Studies of Interactions of TPP-ISA Derivatives with Cyt c

Based on experimental results demonstrating stronger effects of TPP-*6*-ISA vs TPP-*14*-ISA, additional characterization of interactions of TPP-*n*-ISAs with cyt *c* was performed by computer modeling. We performed nineteen simulations with a total duration of 3 μs of cyt *c* and inhibitor complexes and their free forms (Table 1) to characterize the effects of TPP, and the position of imidazole substitution on binding.

Partially unfolded cyt c prefers to fold quickly—As a starting conformation, we used the partially unfolded form of cyt *c* that was utilized in docking studies [6]. In this conformation, red foldon loop (residues 70 to 88) [45] is open and a hydrophobic pocket formed by the heme and red foldon is completely solvent accessible (Fig. 8A, B). We performed two 40 ns long ligand-free simulations to characterize the behavior of the loop in an aqueous environment (supplemental movies 1–2). In both simulations, the inhibitor binding site desolvated and the red foldon loop closed within 3 ns. This fast closing event is due to the high hydrophobicity of the binding pocket and is in accordance with previous studies showing that partial unfolding of the protein and dissociation of Met80 occurs specifically upon CL binding [44, 46].

TPP group has negligible effect on binding of ISA derivatives with CL/cyt c complex—To characterize the effect of the TPP group, we simulated *6*-ISA and TPP-*6*-ISA complex formed in two different binding orientations. In the initial complex configuration, imidazole groups coordinated the heme iron and the aliphatic chains were

elongated parallel to the plane formed by heme (Fig. S1). In 200 ns long simulations, the inhibitor and red foldon loop preferred a compact form to maximize the burial of hydrophobic surface (supplemental movies 2–6). Radius of gyrations of *6*-ISA and TPP-*6*-ISA decreased from 6.8 Å to 4.8 Å and from 9.8 Å to 6.5 Å, respectively. This transition took only 2 to 4 ns. Residues Ile75, Met80, Phe82, Ala83, and Ile85 of the red foldon loop formed interactions with the inhibitors (Table S1). In particular, Met80 and Phe82 enclosed the inhibitors inside the binding site upon closing of the loop. Figure 8C and 8D shows representative configurations for *6*-ISA and TPP-*6*-ISA. Due to the non-specific nature of interactions, we observed multiple potential binding modes for these inhibitors (Fig. 8 and S2). Clustering analysis that excluded the TPP group showed that both inhibitors sampled similar configurations with comparable weights (Fig. S3), suggesting that TPP has a negligible effect on the binding mode of an ISA. The TPP group resided above the binding pocket and interacted with the solvent exposed side of heme (Fig. 8D and supplemental movies 5–6). We also compared the solvent accessible surface area (SASA) of free and bound forms of TPP group (Table 2). Upon binding of TPP-*6*-ISA with cyt *c*, SASA of TPP decreased by 18%, whereas SASA of ISA decreased by 78%, showing that cyt *c* interactions are dominated by hydrophobic ISA group. Similar data were obtained with other TPP-ISA derivatives (Table 2).

TPP-ISA with imidazole substitutions close to carboxylic group more effectively interact with cyt c/CL complex—To evaluate the effect of imidazole substitution position on binding, we performed simulations of free and bound forms of TPP-*n*-ISA series for n =6, 8, 10, 12, and 14 (supplemental movie 7). SASA of bound forms were 53% to 59% smaller than the free form of inhibitors. Longer hydrocarbon chains of inhibitors with the position of imidazole substitutions closer the carboxylic acid (6 and 8) resulted in burial of a larger hydrophobic surface area (Table 2).

Given that the TPP group minimally interacts with the protein, and assuming that the type of imidazole-iron coordination is similar for different analogs, we propose that the major contribution to binding free energy of these compounds comes from desolvation of hydrophobic surfaces of ligand and protein. Free energy of desolvation of hydrocarbons has been shown to correlate with surface area and the contribution of unit area has been reported to range from 20 to 47 cal/mol/$Å^2$ [47–52]. Larger values include corrections for entropic contributions due to molecular size disparity [50, 51]. We calculated relative contribution of desolvation to binding free energy of analogs with respect to TPP-*12*-ISA, which buries the smallest area (Table 2). For TPP-*6*-ISA, the analog with best activity profile, we estimate that relative contribution of desolvation will range from −1.0 to −2.2 kcal/mol.

In vitro Radiomitigation Effects of TPP-n-ISA

We further attempted to validate the significance of the chemical/biochemical and computational predictions using a model of irradiation induced apoptosis in MECs [53] treated with TPP-*n*-ISAs. Two apoptosis hallmarks, *i.e.* PS externalization and caspase-3/7 activation, were assessed. As demonstrated in figure 9, irradiation (10 Gy, 48 hours) induced robust PS externalization (in ~32% of cells) accompanied by activation of caspase-3/7 (~6.5-fold over control cells). Both biomarkers of apoptosis were significantly suppressed

by all the tested TPP-ISA derivatives (5 μM, administrated 30 min after radiation exposure). Among these compounds, TPP-*6*-ISA appeared to be the most potent radiomitigator, resulting in the decreased number of PS-positive cells (~13%, $p < 0.05$) and attenuated capase-3/7 activation (~ 3-fold, $p < 0.05$).

Discussion

In addition to the well know function of mitochondria in bioenergetics, these organelles have also emerged as the major regulatory platform responsible for coordination of numerous metabolic reactions as well as cell death processes. Mitochondrial role in the execution of the program of intrinsic apoptosis includes the production of ROS fueling oxidation of cardiolipin catalyzed by cyt *c* [3–5]. As this oxidation occurs within the peroxidase complex of cyt *c* with CL, the latter represents a promising target for the discovery and design of drugs with anti-apoptotic mechanisms of action.

Under physiological conditions, cyt *c* is located in the intermembrane/intercristae spaces. By way of electrostatic interactions, cyt *c* bounces and shuttles electrons between respiratory complexes III and IV. The axial Fe-S (Met80) bond in native cyt *c* is not very strong and is located in an unstable region (“foldon”) of the protein [54]. Early during intrinsic apoptosis, CL undergoes massive translocation from the inner to the outer mitochondrial membrane thus facilitating its direct physical interactions with intermembrane-space cyt *c* [3]. Combined electrostatic and hydrophobic binding of cyt *c* with CL triggers conformational changes of cyt *c* with the rupture/weakening of the Fe-S-Met bond, transition of hexa-coordinated into penta-coordinated heme iron and the appearance of high-spin state of iron due to the decreased *d*-orbital splitting [3]. This is diagnostic of a partially denatured “molten globule” organization of the heme-protein that is characteristic of many non-native cyt *c* states induced by anionic phospholipids, micelles, polyanions, and electrodes as well as guanidine hydrochloride (GuHCl), low pH, and elevated temperature [55, 56]. These re-arrangements of cyt *c* in the complex with CL are associated with a very strong negative shift of its redox potential (by ~400 mV) resulting in its inability to act as an electron shuttle and switching-on its peroxidase function [57].

We hypothesized that “locking” of the heme-iron coordination bond with a strong ligand delivered through the hydrophobic channel into immediate proximity of the heme catalytic site would suppress the peroxidase activity of CL/cyt *c* complexes, and therefore inhibit the intrinsic apoptosis. Therefore, we designed and synthesized a collection of mitochondria-targeted TPP-*n*-ISA derivatives with a strong Fe ligand - imidazole group - attached to different carbon atoms of their carbon chain. The mitochondrial targeting of TPP-ISA was realized by coupling ISA to a lipophilic TPP cation [6, 58, 59]. The TPP cation has a large, hydrophobic surface area that enables it to pass easily through phospholipid bilayers to be “electrophoresed” and accumulate up to several hundred folds within mitochondria, the site of its action.

By using a combination of absorption and EPR spectroscopies we demonstrated that TPP-*n*-ISA indeed were able to potently suppress CL induced structural re-arrangements in the protein necessary for its action as a peroxidase. TPP-*n*-ISA analogues preserved the low spin

hexa-coordinated heme iron state in CL/cyt *c* complexes whereby TPP-*6*-ISA displayed a significantly more effective preservation than TPP-*14*-ISA. TPP-*6*-ISA decreased the electron density on the porphyrin ring more effectively than the TPP-*14*-ISA as suggested by ESEEM data. Elucidation of these intermolecular stabilization mechanisms of cyt *c* identified TPP-*6*-ISA as an effective inhibitor of the peroxidase function of CL/cyt *c* complexes with a significant anti-apoptotic potential realized in MECs exposed to ionizing irradiation.

These experimental findings were further detailed and confirmed by the computational analysis. All atom simulations suggested that the ISA moiety, rather than the TPP group, was the major contributor to the binding free energy of TPP-ISA. These hydrophobic interactions of TPP-*n*-ISA with heme iron are important in regulation of the ratios of high spin/low spin forms with different symmetry. Imidazole substitution closer to the carboxyl end of the fatty acid chain resulted in burial of a larger hydrophobic surface and produced derivatives that more effectively interacted with cyt *c*/CL complex. The higher anti-peroxidase potency of TPP-*6*-ISA vs TPP-*14*-ISA was also supported by the computational analysis which revealed that TPP-*6*-ISA and TPP-*8*-ISA, with higher buried hydrophobic surface area, were better ligands of TOCL/cyt *c* when compared to TPP-*12*-ISA or TPP-*14*-ISA. These computational interpretations are consistent with previously published EPR data demonstrating the importance of hydrophobic interactions in the lipid-induced modulation of cyt *c* spin states [37]. Addition of more hydrophobic lipids with longer acyl chains increased the content of high spin species of cyt *c*. On the other hand, addition of zwitter-ionic short chain lipids such as dibutyryl PC (C4:0) and didecanoyl PC (C10:0) did not affect the spin state of cyt *c*.

Massive apoptotic cell death resulting in the disruption of essential barriers and tissue and organ failure has been associated with the major pathogenic mechanisms of acute injury. This necessitates the design and development of new anti-apoptotic drugs. Aiming at CL oxidation as a drug target may be particularly promising as it allows for a therapeutic window of several hours from the moment of exposure yet prevents the release of pro-apoptotic factors from mitochondria into the cytosol – an event designating the point-of-no-return in apoptosis [3–5]. Our previous work documented the validity of this approach in acute brain injury (Ji et al., 2012) and acute radiation injury [6]. The effectiveness of TPP-*n*-ISA analogues, particularly TPP-*6*-ISA, as inhibitors of radiation induced programmed cell death may be important for the development of radiomitigative modalities. Indeed, the reality of intentional human exposure to ionizing radiation during radiotherapy and risks of unintended exposure from nuclear accidents, unavoidable occupational environments, as well as exposures during space exploration or potential terroristic attacks necessitates design and development of effective protective/mitigative modalities. This requires profound understanding of the mechanisms of radiation-induced damage. High doses of irradiation induce acute radiation syndrome associated with massive cell loss in radiosensitive organs, believed to be mostly due to triggering of intrinsic, mitochondria-mediated, apoptosis [60]. This emphasizes the importance of the identification of TPP-*6*-ISA as a candidate drug with optimized radiomitigative potency.

Supplementary Material

Refer to Web version on PubMed Central for supplementary material.

Acknowledgments

This work is supported by the National Institutes of Health grants (U19AIO68021, P01 HL114453, ES020693, ES021068, GM099738-02); National Science Foundation grant (MCB 1157712); and the Fulbright Canada award (VEK).

References

1. Orrenius S. Reactive oxygen species in mitochondria-mediated cell death. Drug Metab Rev. 2007; 39:443–455. [PubMed: 17786631]
2. Fruehauf JP, Meyskens FL Jr. Reactive oxygen species: a breath of life or death? Clin Cancer Res. 2007; 13:789–794. [PubMed: 17289868]
3. Kagan VE, Tyurin VA, Jiang JF, Tyurina YY, Ritov VB, Amoscato AA, Osipov AN, Belikova NA, Kapralov AA, Kini V, Vlasova II, Zhao Q, Zou MM, Di P, Svistunenko DA, Kurnikov IV, Borisenko GG. Cytochrome c acts as a cardiolipin oxygenase required for release of proapoptotic factors. Nat Chem Biol. 2005; 1:223–232. [PubMed: 16408039]
4. Gonzalvez F, Gottlieb E. Cardiolipin: setting the beat of apoptosis. Apoptosis. 2007; 12:877–885. [PubMed: 17294083]
5. Ott M, Gogvadze V, Orrenius S, Zhivotovsky B. Mitochondria, oxidative stress and cell death. Apoptosis. 2007; 12:913–922. [PubMed: 17453160]
6. Atkinson J, Kapralov AA, Yanamala N, Tyurina YY, Amoscato AA, Pearce L, Peterson J, Huang Z, Jiang J, Samhan-Arias AK, Maeda A, Feng W, Wasserloos K, Belikova NA, Tyurin VA, Wang H, Fletcher J, Wang Y, Vlasova, Klein-Seetharaman J, Stoyanovsky DA, Bayir H, Pitt BR, Epperly MW, Greenberger JS, Kagan VE. A mitochondria-targeted inhibitor of cytochrome c peroxidase mitigates radiation-induced death. Nature communications. 2011; 2:497.
7. Ji J, Kline AE, Amoscato A, Samhan-Arias AK, Sparvero LJ, Tyurin VA, Tyurina YY, Fink B, Manole MD, Puccio AM, Okonkwo DO, Cheng JP, Alexander H, Clark RS, Kochanek PM, Wipf P, Kagan VE, Bayir H. Lipidomics identifies cardiolipin oxidation as a mitochondrial target for redox therapy of brain injury. Nature neuroscience. 2012; 15:1407–1413.
8. Jiang J, Kurnikov I, Belikova NA, Xiao J, Zhao Q, Amoscato AA, Braslau R, Studer A, Fink MP, Greenberger JS, Wipf P, Kagan VE. Structural requirements for optimized delivery, inhibition of oxidative stress, and antiapoptotic activity of targeted nitroxides. J Pharmacol Exp Ther. 2007; 320:1050–1060. [PubMed: 17179468]
9. Jiang J, Stoyanovsky DA, Belikova NA, Tyurina YY, Zhao Q, Tungekar MA, Kapralova V, Huang Z, Mintz AH, Greenberger JS, Kagan VE. A mitochondria-targeted triphenylphosphonium-conjugated nitroxide functions as a radioprotector/mitigator. Radiat Res. 2009; 172:706–717. [PubMed: 19929417]
10. Ogura A, Oowada S, Kon Y, Hirayama A, Yasui H, Meike S, Kobayashi S, Kuwabara M, Inanami O. Redox regulation in radiation-induced cytochrome c release from mitochondria of human lung carcinoma A549 cells. Cancer Lett. 2009; 277:64–71. [PubMed: 19117669]
11. Chu CT, Ji J, Dagda RK, Jiang JF, Tyurina YY, Kapralov AA, Tyurin VA, Yanamala N, Shrivastava IH, Mohammadyani D, Qiang Wang KZ, Zhu J, Klein-Seetharaman J, Balasubramanian K, Amoscato AA, Borisenko G, Huang Z, Gusdon AM, Cheikhi A, Steer EK, Wang R, Baty C, Watkins S, Bahar I, Bayir H, Kagan VE. Cardiolipin externalization to the outer mitochondrial membrane acts as an elimination signal for mitophagy in neuronal cells. Nature cell biology. 2013; 15:1197–1205.
12. Kagan VE, Bayir HA, Belikova NA, Kapralov O, Tyurina YY, Tyurin VA, Jiang JF, Stoyanovsky DA, Wipf P, Kochanek PM, Greenberger JS, Pitt B, Shvedova AA, Borisenko G. Cytochrome c/cardiolipin relations in mitochondria: a kiss of death. Free Radical Bio Med. 2009; 46:1439–1453. [PubMed: 19285551]

13. Li K, Li YC, Shelton JM, Richardson JA, Spencer E, Chen ZJ, Wang XD, Williams RS. Cytochrome c deficiency causes embryonic lethality and attenuates stress-induced apoptosis. Cell. 2000; 101:389–399. [PubMed: 10830166]
14. Florence TM. The Degradation of Cytochrome-C by Hydrogen-Peroxide. J Inorg Biochem. 1985; 23:131–141. [PubMed: 2983016]
15. Radi R, Thomson L, Rubbo H, Prodanov E. Cytochrome-C-Catalyzed Oxidation of Organic-Molecules by Hydrogen-Peroxide. Arch Biochem Biophys. 1991; 288:112–117. [PubMed: 1654817]
16. Tuominen EKJ, Wallace CJA, Kinnunen PKJ. Phospholipid-cytochrome c interaction - Evidence for the extended lipid anchorage. Journal of Biological Chemistry. 2002; 277:8822–8826. [PubMed: 11781329]
17. Chattopadhyay K, Mazumdar S. Stabilization of partially folded states of cytochrome C in aqueous surfactant: effects of ionic and hydrophobic interactions. Biochemistry-Us. 2003; 42:14606–14613.
18. Murphy MP, Smith RA. Targeting antioxidants to mitochondria by conjugation to lipophilic cations. Annual review of pharmacology and toxicology. 2007; 47:629–656.
19. Claus RE, Schreiber SL. Ozonolytic cleavage of cyclohexen to terminally differentiated products: methyl 6-oxohexanoate, 6,6-dimethylhexanal, methyl 6,6-dimethoxyhexanoate. Organic Syntheses. 1986; 64:150–153.
20. Taber DF, Nakajima K. Unsymmetrical ozonolysis of a Diels-Alder adduct: Practical preparation of a key intermediate for heme total synthesis. Journal of Organic Chemistry. 2001; 66:2515–2517. [PubMed: 11281801]
21. Bouzide A, Sauve G. Highly selective silver(I) oxide mediated monoprotection of symmetrical diols. Tetrahedron Letters. 1997; 38:5945–5948.
22. Corey EJ, Suggs JW. Pyridinium Chlorochromate - Efficient Reagent for Oxidation of Primary and Secondary Alcohols to Carbonyl-Compounds. Tetrahedron Letters. 1975:2647–2650.
23. Fauth JM, Schweiger A, Braunschweiler L, Forrer J, Ernst RR. Elimination of unwanted echoes and reduction of dead time in three-pulse electron spin-echo spectroscopy. Journal of Magnetic Resonance. 1986; 66:74–85.
24. Gemperle C, Aebli G, Schweiger A, Ernst RR. Phase cycling in pulse EPR. Journal of Magnetic Resonance. 1990; 88:241–256.
25. Phillips JC, Braun R, Wang W, Gumbart J, Tajkhorshid E, Villa E, Chipot C, Skeel RD, Kale L, Schulten K. Scalable molecular dynamics with NAMD. J Comput Chem. 2005; 26:1781–1802. [PubMed: 16222654]
26. MacKerell, AD.; Brooks, B.; Brooks, CL.; Nilsson, L.; Roux, B.; Won, Y.; Karplus, M. Encyclopedia of Computational Chemistry. John Wiley & Sons, Ltd; 2002. CHARMM: The Energy Function and Its Parameterization.
27. Autenrieth F, Tajkhorshid E, Baudry J, Luthey-Schulten Z. Classical force field parameters for the heme prosthetic group of cytochrome c. J Comput Chem. 2004; 25:1613–1622. [PubMed: 15264255]
28. Pastor RW, MacKerell AD. Development of the CHARMM Force Field for Lipids. J Phys Chem Lett. 2011; 2:1526–1532. [PubMed: 21760975]
29. Pettersen EF, Goddard TD, Huang CC, Couch GS, Greenblatt DM, Meng EC, Ferrin TE. UCSF chimera - A visualization system for exploratory research and analysis. J Comput Chem. 2004; 25:1605–1612. [PubMed: 15264254]
30. Bakan A, Meireles LM, Bahar I. ProDy: protein dynamics inferred from theory and experiments. Bioinformatics. 2011; 27:1575–1577. [PubMed: 21471012]
31. Humphrey W, Dalke A, Schulten K. VMD: Visual molecular dynamics. J Mol Graph Model. 1996; 14:33–38.
32. Marques HM. Insights into porphyrin chemistry provided by the microperoxidases, the haempeptides derived from cytochrome c. Dalton T. 2007:4371–4385.
33. Munro OQ, Marques HM. Heme-peptide models for hemoproteins 1. Solution chemistry of N-acetylmicroperoxidase-8. Inorg Chem. 1996; 35:3752–3767. [PubMed: 11666562]

34. Antonini, E.; Brunori, M. The derivatives of ferric hemoglobin and myoglobin. In: Neuberger, A.; Tatum, EL., editors. Hemoglobin and myoglobin in their reactions with ligands. North-Holland Pub. Co; 1971.
35. Carraway AD, McCollum MG, Peterson J. Characterization of N-acetylated heme undecapeptide and some of its derivatives in aqueous media: Monomeric model systems for hemoproteins. Inorg Chem. 1996; 35:6885–6891. [PubMed: 11666857]
36. Brautigan DL, Feinberg BA, Hoffman BM, Margoliash E, Preisach J, Blumberg WE. Multiple low spin forms of the cytochrome c ferrihemochrome. EPR spectra of various eukaryotic and prokaryotic cytochromes c. The Journal of biological chemistry. 1977; 252:574–582. [PubMed: 13072]
37. Zucchi MR, Nascimento OR, Faljoni-Alario A, Prieto T, Nantes IL. Modulation of cytochrome c spin states by lipid acyl chains: a continuous-wave electron paramagnetic resonance (CW-EPR) study of haem iron. The Biochemical journal. 2003; 370:671–678. [PubMed: 12429017]
38. Deligiannakis Y, Rutherford AW. Effect of pH on the semiquinone radical Q(A)- in CN-treated photosystem II: study by hyperfine sublevel correlation spectroscopy. Journal of inorganic biochemistry. 2000; 79:339–345. [PubMed: 10830886]
39. Peisach J, Mims WB, Davis JL. Studies of the electron-nuclear coupling between Fe(III) and 14N in cytochrome P-450 and in a series of low spin heme compounds. The Journal of biological chemistry. 1979; 254:12379–12389. [PubMed: 227893]
40. Theodorakis JL, Garber EA, McCracken J, Peisach J, Schejter A, Margoliash E. A chemical modification of cytochrome-c lysines leading to changes in heme iron ligation. Biochimica et biophysica acta. 1995; 1252:103–113. [PubMed: 7548152]
41. Stoll S, Calle C, Mitrikas G, Schweiger A. Peak suppression in ESEEM spectra of multinuclear spin systems. Journal of Magnetic Resonance. 2005; 177:93–101. [PubMed: 16112885]
42. Britt RD, Campbell KA, Peloquin JM, Gilchrist ML, Aznar CP, Dicus MM, Robblee J, Messinger J. Recent Pulsed EPR Studies of the Photosystem II Oxygen-Evolving Complex: Implication as to Water Oxidation Mechanisms. Biochimica et Biophysica Acta. 2004; 1655:158–171. [PubMed: 15100028]
43. Deligiannakis Y, Louloudi M, Hadjiliadis N. Electron spin echo envelope modulation (ESEEM) spectroscopy as a tool to investigate the coordination environment of metal centers. Coordin Chem Rev. 2000; 204:1–112.
44. Hanske J, Toffey JR, Morenz AM, Bonilla AJ, Schiavoni KH, Pletneva EV. Conformational properties of cardiolipin-bound cytochrome c. Proceedings of the National Academy of Sciences of the United States of America. 2012; 109:125–130. [PubMed: 22190488]
45. Maity H, Maity M, Krishna MMG, Mayne L, Englander SW. Protein folding: The stepwise assembly of foldon units. P Natl Acad Sci USA. 2005; 102:4741–4746.
46. Sinibaldi F, Fiorucci L, Patriarca A, Lauceri R, Ferri T, Coletta M, Santucci R. Insights into cytochrome c-cardiolipin interaction, Role played by ionic strength. Biochemistry-Us. 2008; 47:6928–6935.
47. Reynolds JA, Gilbert DB, Tanford C. Empirical Correlation between Hydrophobic Free-Energy and Aqueous Cavity Surface-Area. P Natl Acad Sci USA. 1974; 71:2925–2927.
48. Hermann RB. Theory of Hydrophobic Bonding 2. Correlation of Hydrocarbon Solubility in Water with Solvent Cavity Surface-Area. J Phys Chem-Us. 1972; 76:2754.
49. Hermann RB. Use of Solvent Cavity Area and Number of Packed Solvent Molecules around a Solute in Regard to Hydrocarbon Solubilities and Hydrophobic Interactions. P Natl Acad Sci USA. 1977; 74:4144–4145.
50. Deyoung LR, Dill KA. Partitioning of Nonpolar Solutes into Bilayers and Amorphous N-Alkanes. J Phys Chem-Us. 1990; 94:801–809.
51. Sharp KA, Nicholls A, Fine RF, Honig B. Reconciling the magnitude of the microscopic and macroscopic hydrophobic effects. Science. 1991; 252:106–109. [PubMed: 2011744]
52. Cheng AC, Coleman RG, Smyth KT, Cao Q, Soulard P, Caffrey DR, Salzberg AC, Huang ES. Structure-based maximal affinity model predicts small-molecule druggability. Nat Biotechnol. 2007; 25:71–75. [PubMed: 17211405]

53. Jiang JF, Belikova NA, Hoye AT, Zhao Q, Epperly MW, Greenberger JS, Wipf P, Kagan VE. A mitochondria-targeted nitroxide/hemigramicidin S conjugate protects mouse embryonic cells against gamma irradiation. Int J Radiat Oncol. 2008; 70:816–825.

54. Telford JR, Tezcan FA, Gray HB, Winkler JR. Role of ligand substitution in ferrocytochrome c folding. Biochemistry. 1999; 38:1944–1949. [PubMed: 10026276]

55. Battistuzzi G, Bortolotti CA, Bellei M, Di Rocco G, Salewski J, Hildebrandt P, Sola M. Role of Met80 and Tyr67 in the Low-pH Conformational Equilibria of Cytochrome c. Biochemistry-Us. 2012; 51:5967–5978.

56. Oellerich S, Wackerbarth H, Hildebrandt P. Spectroscopic characterization of nonnative conformational states of cytochrome c. J Phys Chem B. 2002; 106:6566–6580.

57. Basova LV, Kurnikov IV, Wang L, Ritov VB, Belikova NA, Vlasova, Pacheco AA, Winnica DE, Peterson J, Bayir H, Waldeck DH, Kagan VE. Cardiolipin switch in mitochondria: shutting off the reduction of cytochrome c and turning on the peroxidase activity. Biochemistry. 2007; 46:3423–3434. [PubMed: 17319652]

58. Brown SE, Ross MF, Sanjuan-Pla A, Manas AR, Smith RA, Murphy MP. Targeting lipoic acid to mitochondria: synthesis and characterization of a triphenylphosphonium-conjugated alpha-lipoyl derivative. Free radical biology & medicine. 2007; 42:1766–1780. [PubMed: 17512456]

59. Ross MF, Prime TA, Abakumova I, James AM, Porteous CM, Smith RA, Murphy MP. Rapid and extensive uptake and activation of hydrophobic triphenylphosphonium cations within cells. The Biochemical journal. 2008; 411:633–645. [PubMed: 18294140]

60. Dewey WC, Ling CC, Meyn RE. Radiation-induced apoptosis: relevance to radiotherapy. Int J Radiat Oncol Biol Phys. 1995; 33:781–796. [PubMed: 7591884]

Highlights

- Mitochondria-targeted imidazole-substituted stearic acids was synthesized.
- TPP-*n*-ISAs suppressed cardiolipin-induced structural rearrangements in cytochrome *c*.
- TPP-*n*-ISAs preserved the low spin hexa-coordinated heme iron state in cytochrome *c*.
- TPP-*n*-ISAs inhibited the peroxidase activity of cytochrome c/cardiolipin complex.
- TPP-*6*-ISA was identified as an optimized candidate anti-apoptotic drug.

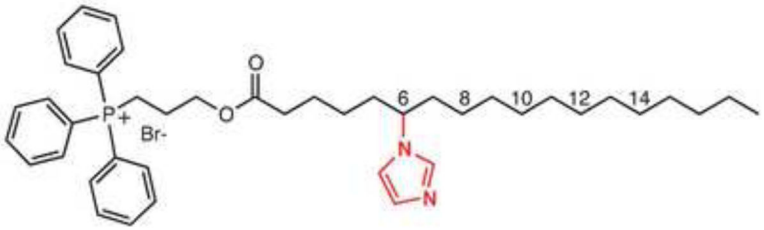

Fig. 1.
Chemical structure of TPP-conjugated-*6*-imidazole-substituted stearic acid.

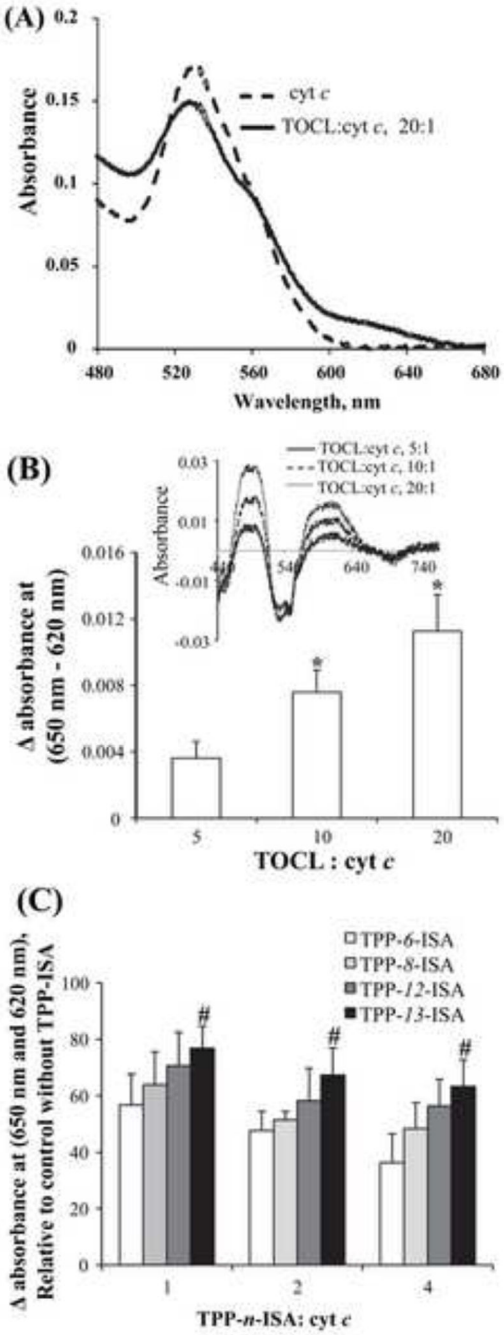

Fig. 2.

Absorption spectra of cyt *c* illustrating inhibition of TOCL-dependent formation of its heme iron high-spin form by TPP-ISA derivatives. (A) Absorption spectra of cyt *c* (75 μM) in the presence of TOCL (TOCL:cyt *c*, 20:1). (B) Effect of TOCL (TOCL/cyt *c* ratio (5:1, 10:1, and 20:1) on the formation of high-spin iron. For quantitative assessment of the formation of high- spin iron, the height of peak at *ca.* 620 nm was calculated by subtraction of absorbance reading at 675 nm from that at 620 nm. *Insert* - the differential absorbance spectrum created by subtracting the spectra of cyt *c* from the spectra of TPCL/cyt *c* complex. (C) Effect of

TPP-ISA on TOCL-dependent formation of high-spin form of cyt *c* heme iron. Spectra were recorded in 20 mM HEPES buffer (pH 7.4) containing 75 μM cyt *c* and 100 μM DTPA. Data presented are means ± SD (n=6). * $p < 0.05$ *vs* TOCL/cyt *c* ratio of 5:1, # $p < 0.05$ *vs* TPP-6-ISA under the same experimental condition.

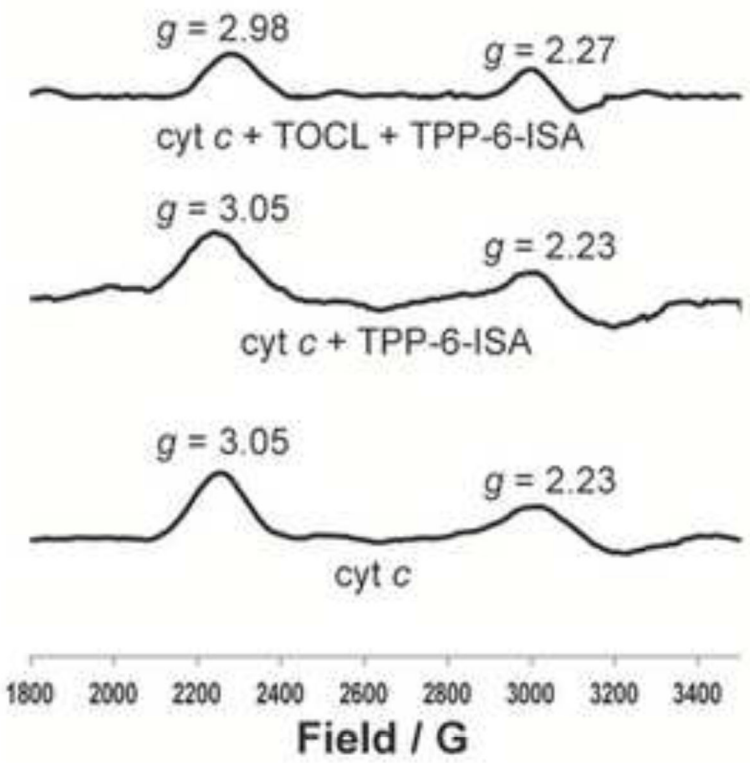

Fig. 3.

CW-EPR spectra of the heme iron signals in cyt *c*. Experiments were conducted at a temperature of 10 K. The concentration of cyt *c* was 500 μM and the ratio of cyt *c*:TPP-*n*-ISA:TOCL was 1:1:20. The peaks around g ~3.07 and g ~ 2.24 correspond to a low spin state of the heme iron. Changes in the g values upon the addition of TPP-*n*-ISAs to cyt *c*/TOCL complex are consistent with the ligation of His/Imidazole to heme center.

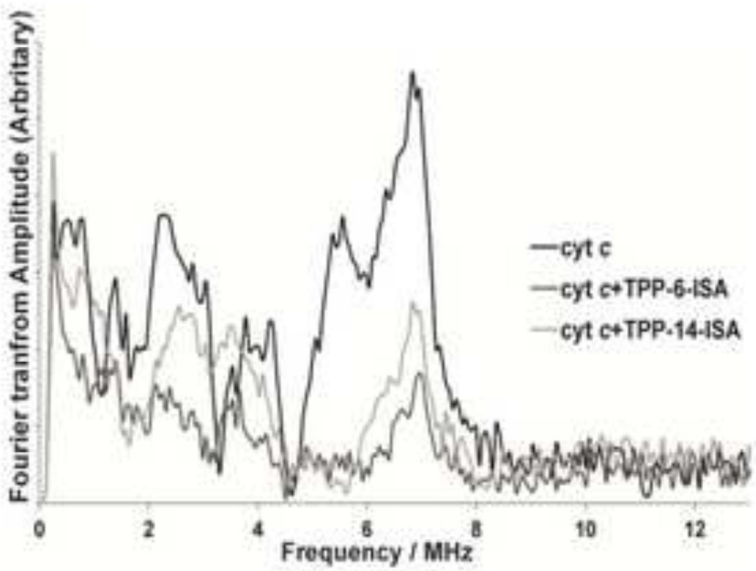

Fig. 4.

ESEEM spectra showing the interaction of TPP-*n*-ISA with cyt *c*. The ESEEM experiments were conducted at 4.2 K, using a pulse sequence of π/2-τ-π/2- T-π/2-echo with a π/2 pulse length of 16 ns. Note that TPP-*6*-ISA interacts more effectively with the heme center compared to TPP-*14*-ISA.

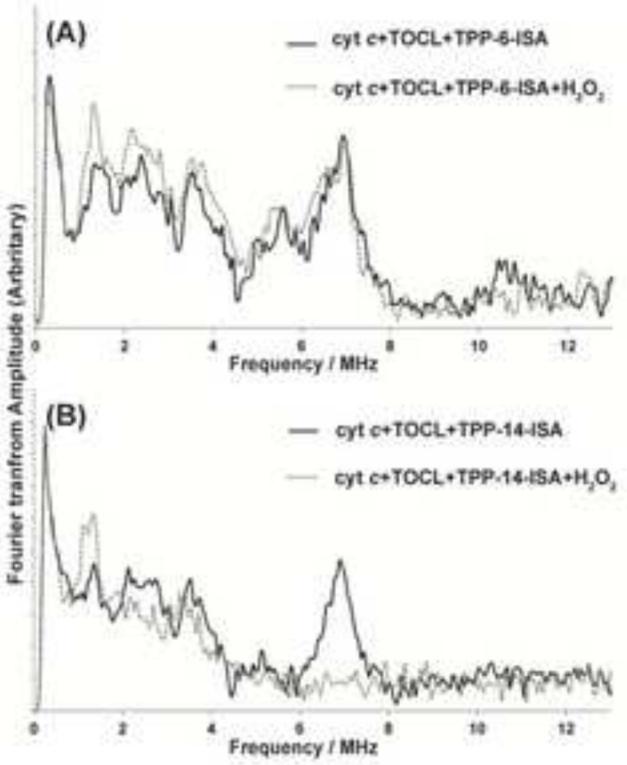

Fig. 5.

ESEEM spectra of cyt *c* in the presence of TOCL and TPP-*n*-ISA. The experiments were carried out at 4.2 K, using a pulse sequence of π/2-τ-π/2- T-π/2-echo with a π/2 pulse length of 16 ns. The ratio of cyt *c*: TOCL was 1:20 with a cyt *c* concentration of 500 μM. The ratio between cyt *c* and TPP-*n*-ISA was 1:1 and nine equivalents of H_2O_2 were added for the H_2O_2 experiments. (A) Upon the addition of H_2O_2 the spectral features remained the same for TPP-*6*-ISA. (B) For TPP-*14*-ISA, upon the addition of H_2O_2 the feature around 6.8 MHz was no longer present (dashed spectra).

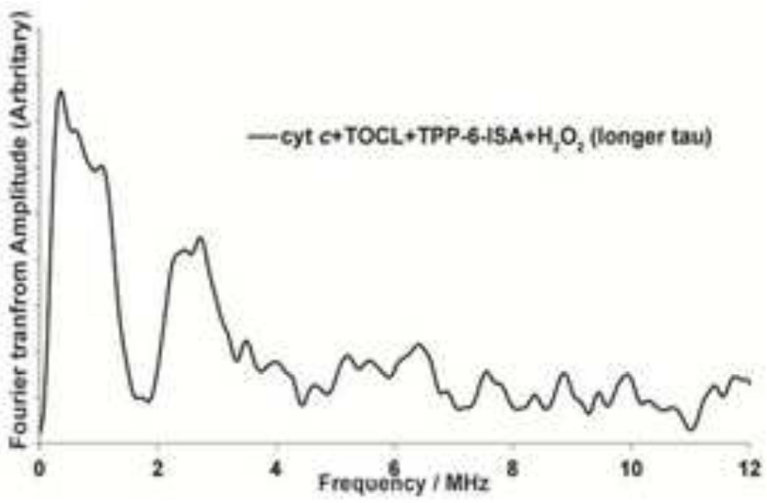

Fig. 6.

ESEEM spectra of the cyt *c*/TOCL complex in the presence of TPP-6-ISA and H_2O_2 with a pulse separation of 288 ns. At longer pulse separations the low frequency features corresponding to imidazole coordination (0.4, 1.7 and 2.2 MHz) are clearly visible.

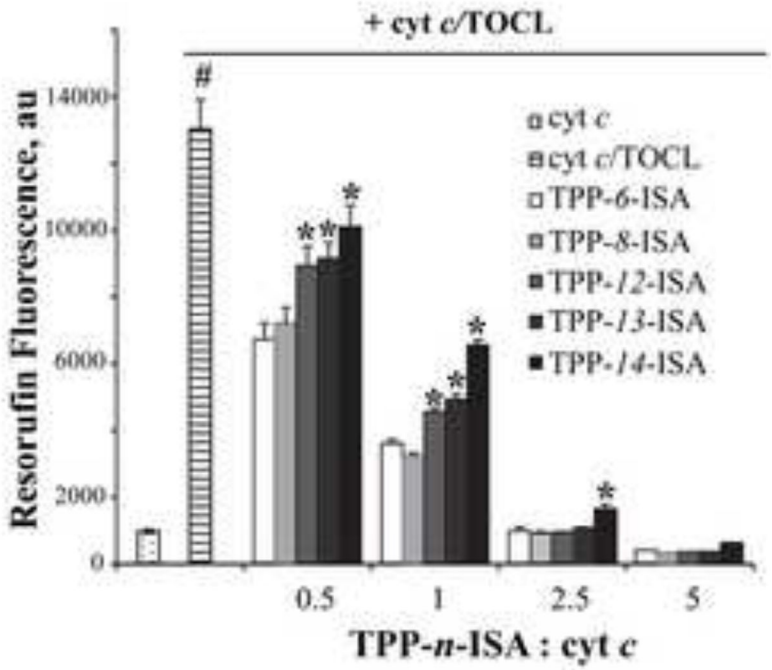

Fig. 7.

Inhibition of peroxidase activity of TOCL/cyt *c* complexes by TPP-*n*-ISA. Peroxidase activity was evaluated by determining the H_2O_2-dependent oxidation of Amplex Red. Data presented are means ± SD (n=6), # $p < 0.05$ *vs* cyt *c* alone, * $p < 0.05$ *vs* TPP-*6*-ISA under the same condition.

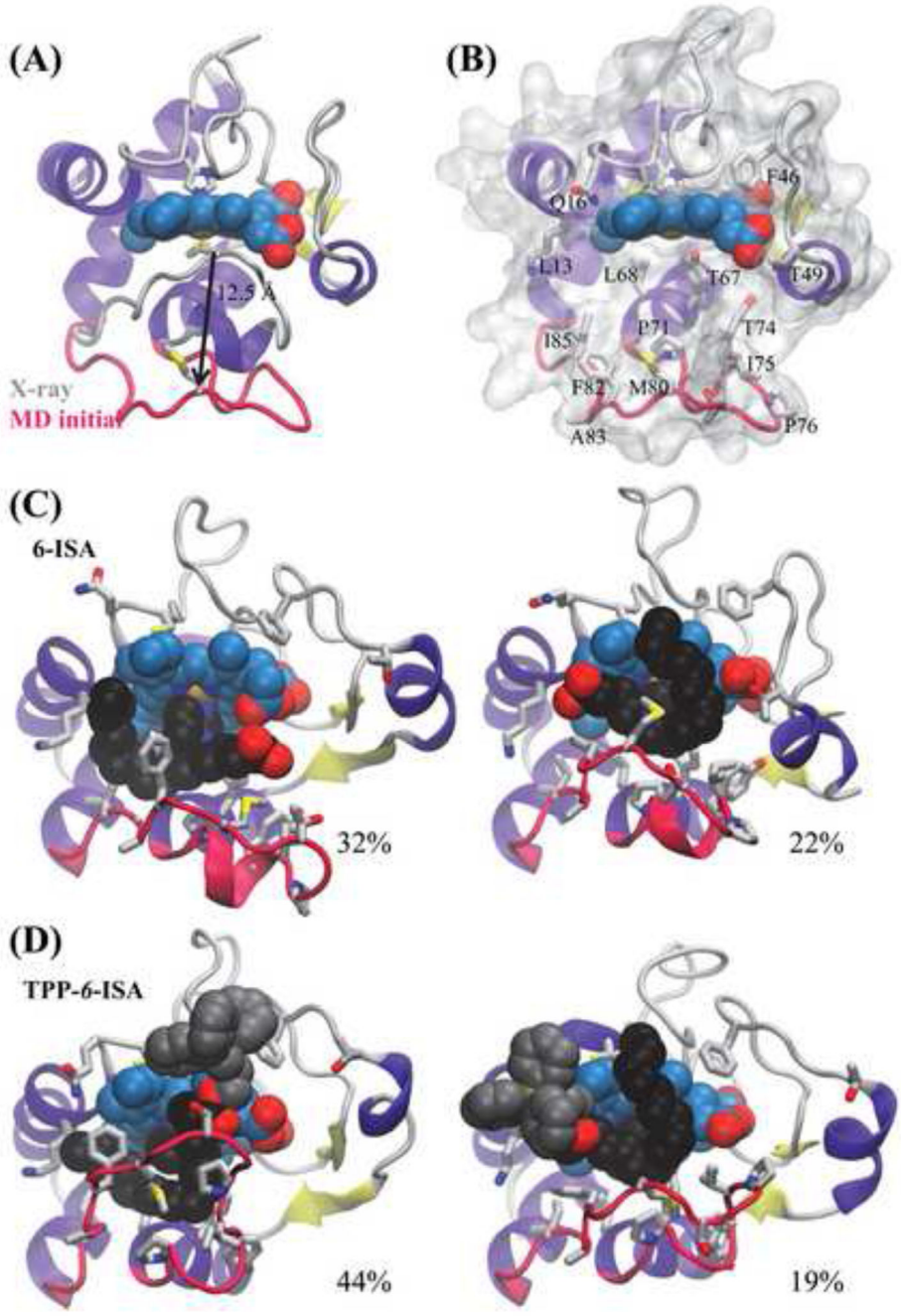

Fig. 8.

Cyt *c* structure and inhibitor interactions. (A) Crystal structure of cyt *c* is compared to the partially unfolded conformation used in MD simulations. Residues Asn70 to Lys88 that form the red loop foldon bear an open conformation, whereby Met80 is 12.5 Å away from its position in the crystal structure. (B) Initial conformation is displayed in surface representation to show binding site residues. All residues that interact with inhibitors in at least 20% of the simulation duration are labeled. Tyr67, Leu68, Pro71, and I75 inlay the binding pocket. See Table S1 for details. (C–D). Most frequently observed *6*-ISA and

TPP-*6*-ISA binding modes are shown. Red loop foldon tends to close over bound inhibitors. In particular, Met80 and Phe82 side-chains interact closely with the inhibitors and hold them in position. TPP group (grey) resides outside of the binding pocket and does not have a significant effect on ISA binding mode. For alternate binding modes and full-length movies of the simulations, see supplementary figures and movies.

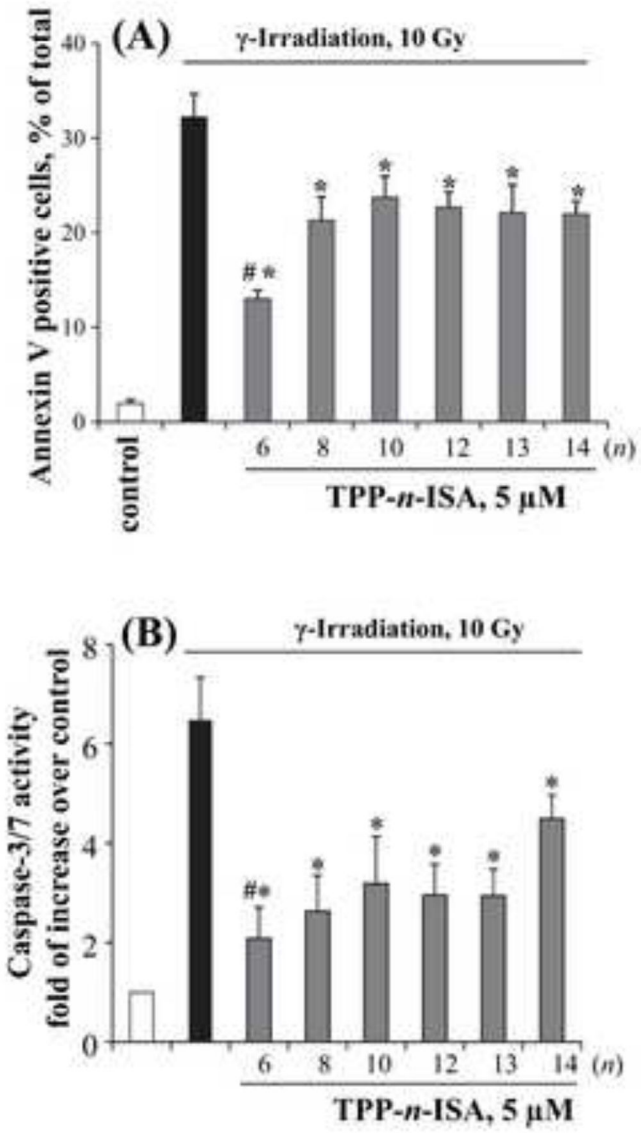

Fig. 9.

Mitigative effects of TPP-*n*-ISAs against irradiation induced cell death. Cells were γ-irradiated at a dose of 10 Gy, and then incubated in the presence (added 30 min post-irradiation) or absence of 5 μM TPP-*n*-ISAs for 48 hours. After that, cells were collected for apoptosis analysis. (A) Determination of PS externalization with flow cytometry using an Annexin V-FITC/PI kit. (B) Measurement of Caspase-3/7 activation using a luminescence Caspase-Glo 3/7 assay kit. Data are mean ± SD, n=3. * $p < 0.05$ *vs* irradiated cells without TPP-ISA treatment, # $p < 0.05$ vs TPP-*14*-ISA

Table 1

Summary of simulations.

	Complex	Free
cyt *c*		40 ns × 2
6-ISA	200 ns × 2	
TPP-*6*-ISA	200 ns × 2	100 ns
TPP-*8*-ISA	200 ns × 2	100 ns
TPP-*10*-ISA	200 ns × 2	100 ns
TPP-*12*-ISA	200 ns × 2	100 ns
TPP-*14*-ISA	200 ns × 2	100 ns

Table 2

Solvent accessible surface area (SASA)

	SASA (Å^2) in free form			SASA (Å^2) in bound form				
n	**All atoms**	**TPP**[1]	**ISA**[1]	**All atoms**[2]	**TPP**[2]	**ISA**[2]	**$\Delta SASA_{ISA}$**	**$\Delta\Delta G_{desolvation}$**[3] **(kcal/mol)**
6	1019 ± 88	370 ± 40	435 ± 47	449 ± 79 (56%)	303 ± 51 (18%)	95 ± 49 (78%)	340	−1.0 to −2.2
8	1045 ± 80	380 ± 37	441 ± 40	429 ± 73 (59%)	273 ± 55 (28%)	99 ± 29 (78%)	342	−1.1 to −2.3
10	1010 ± 91	367 ± 41	422 ± 44	440 ± 81 (56%)	288 ± 51 (22%)	101 ± 45 (76%)	321	−0.7 to −1.4
12	1014 ± 96	364 ± 45	422 ± 45	476 ± 87 (53%)	249 ± 77 (32%)	134 ± 29 (68%)	288	0.0
14	1027 ± 94	369 ± 45	427 ± 43	485 ± 77 (53%)	278 ± 71 (25%)	126 ± 44 (70%)	301	−0.3 to −0.6

[1] TPP and ISA carbon atoms are considered for SASA calculations.

[2] Percentage of exposed surface area with respect to the free form is shown in parentheses.

[3] Relative contribution of desolvation to binding free energies are reported with respect to TPP-*12*-ISA. Range is calculated using lower and upper limits of per area contributions reported by *Reynolds* [47] and *Sharp et al.*[51].